Available online www.jocpr.com

Journal of Chemical and Pharmaceutical Research, 2016, 8(11):266-278

Research Article

ISSN : 0975-7384
CODEN(USA) : JCPRC5

Analytical Investigation of Nanofluid Natural Convection in a Shallow Cavity with Differentially Heated End Walls in Presence of Electromagnetic Forces

Ahmad Jamali Keikha

Chabahar Maritime University, Chabahar, Iran

ABSTRACT

The present study deals with the effect of electromagnetic forces on the problem of natural convection in a cavity of small aspect ratio with differentially heated end walls. It is shown by use of matched asymptotic expansions that the flow consists of two distinct regimes: a parallel flow in the core region and a second, non-parallel flow near the ends of the cavity. A solution valid at all orders in the aspect ratio A is found for the core region, while the first several terms of the appropriate asymptotic expansion are obtained for the end regions. Parametric limits of validity for the parallel flow structure are discussed. Asymptotic expressions for the Nusselt number and the single free parameter of the parallel flow solution, valid in the limit as A→ 0, are derived.

Keywords: Magnetohydrodynamics; Analytical solution; Natural convection; Laminar flow; Boundary layer

---

INTRODUCTION

Magnetic field plays a significant role for an external thermal control in many industries, associated to liquid metals and high-energy equipment [1,2]. The presence of magnetic field can reduce turbulent flows and fluctuations during the solidification process [3]. Because of strong effect of magnetic field on convective flows and heat transfer it uses in liquid metal blankets, crystal growth and other industries [1], [2] and [3]. Analysis of MHD convective fluid flow and heat transfer is presented in many papers [4-10]. Thus, Sathiyamoorthy and Chamkha [4] have studied numerically natural convective flow and heat transfer of electrically conducting liquid gallium in a square cavity under the effect of inclined uniform magnetic field. It has been found that the average Nusselt number is a non-linear decreasing function of the Hartmann number regardless of the magnetic field inclination angle. Benos et al. [5] have analyzed steady two-dimensional MHD natural convection of an electrically conducting fluid in a horizontal internally heated shallow cavity. Numerical study has been carried out using a finite volume technique. They found that the fluid is decelerated by the magnetic field leading to the dominance of heat conduction and the heat transfer reduction. MHD natural convective flow and heat transfer in a laterally heated enclosure with a heat-conducting vertical partition on the basis of polynomial differential quadrature method has been investigated by Kahveci and Oztuna [6]. It has been found that the x-directional magnetic field is more effective in suppression of convection than the y-directional magnetic field. Jing et al. [7] have studied MHD natural convection of liquid metal in a cubical cavity using the projection method of second-order accuracy. It has been shown that three-dimensional effects on temperature are much stronger when the cavity walls are heat-conducting compared with the temperature distribution in the case of adiabatic walls. Numerical simulation of steady buoyant flow of liquid LiPb in a cubical cavity under the effect of magnetic field has been carried out by Wang et al. [8] using Fluent software. It has been shown that for high values of Hartmann number the control effects of magnetic field on convective motion become visible and the velocity profiles tend to become uniform. Numerical and experimental analysis of natural convection in a cubical cavity filled with a magnetic fluid under the effect of uniform magnetic field has been carried out by

Yamaguchi et al. [9] and Krakov et al. [10]. The obtained results showed that a set of numerous convective structures exists in the cube and stability of these structures depends on the interaction between gravity and Lorentz forces. Bondareva and Sheremet [11] have analyzed laminar natural convection of metal melt (Pr = 0.02) in a three-dimensional enclosure under the effect of inclined uniform magnetic field. It has been shown that it is possible to utilize 2D data for an analysis of average Nusselt number when the aspect ratio (A) is greater than unit while the flow configuration in the mid-section of a 3D cavity differs insignificantly only than A≥2. Selimefendigil et al. [12] have studied natural convective heat transfer of ferrofluid in a partially heated square cavity. It has been revealed that velocity profiles are very sensitive to the magnetic dipole source strength and the average heat transfer decreases with the magnetic dipole strength. Now many studies deal with analysis of MHD natural convection in nanofluids [13-15].

Not so many theoretical and even less experimental investigations are dedicated to the problem of natural convection regimes during phase transition under the influence of external magnetic field [16,17]. Thus, Bouabdallah and Bessaih [16] have analyzed the effect of magnetic field on three-dimensional natural convection solidification in a cubical cavity. The finite volume method with enthalpy formulation is utilized to solve the formulated boundary value problem. It has been found a strong dependence between the solid–liquid interface shape and the intensity and orientation of magnetic field. Zaidat et al. [17] have conducted experiments on control of melt convection by a traveling electromagnetic field. Some investigations have been carried out on melting of phase change material in various cavities [18-20] in the absence of magnetic field effects.

The purpose of the present study is to examine the influence of inclined magnetic field on natural convection melting in a cavity with a local heater. Calculations have been performed for a square enclosure filled with pure gallium heated from the local source and cooled from two vertical side walls. The present paper is an extension of natural convection melting without magnetic field [20]. To authors best of knowledge this problem has not been studied before and the reported results are new and original.

EXPERIMENTAL SECTION

The schematic view of the experimental setup is depicted in Fig. 1. The setup was categorized into three parts; namely (i) open circuit wind tunnel system, (ii) test section, and (iii) data acquisition system. The working fluid (air) was provided with the help of an 18.5 kW radial fan. The desired air flow rate can be controlled using a frequency converter by changing the speed of the radial fan. Compressed air from the radial fan primarily passed from the flow regulator (straightener) to the test section and is then thrown into the environment. Air flow rate was measured both at the fan outlet and at the end of the test section due to the risk of leakage of the designated test section. Two different probes for laminar and turbulent flow conditions were used due to the limited measurement range of the probes. Kimo LV101 (accuracy; %3 for 0.8–3 m/s, %1 for 3.1–25 m/s) for laminar flow, Kimo LV107 (accuracy; %3 for 0.3–3 m/s, %1 for 3.1–35 m/s) for turbulent flow were used as an anemometer. Heat transfer experiments were conducted with 10 different air flow rates for laminar flow and 8 different air flow rates for turbulent flow. Pressure drop experiments were conducted with 22 different air flow rates for laminar flow and in the same manner, 8 different air flow rates for turbulent flow. Heat transfer and the pressure drop experiments were repeated 4–5 times consecutively.

Consider a square cavity of length L with a square heat source of sizelhaving high constant temperature Th mounted on the bottom wall. At initial time the cavity is filled with a phase change material (pure gallium) in solid state having fusion temperature Tm. Two opposite vertical walls are kept at low constant temperature Tc. Uniform magnetic field affects the natural convective melt flow and heat transfer under the inclination angle α. The schematic diagram of the physical system with temperature boundary conditions is presented in Figure 1.

Here the drug delivery from the body to the cellular scale in animal and human clinical trials is studied by magnetic resonance (MR) image for a cancer patient where magnetic nano-particle accumulate as lighter regions at the arrow tips (due to the MR extinction phenomena). Magneto-particle can concentrated in rabbit tumor micro-vessels or at the membrane of mouse epithelial cells.

Governing equations including for bio-fluid, blood with magnetic Nano-particles, in x and y direction are as follows:

$$u = \frac{\partial \Psi^*}{\partial y} \qquad v = -\frac{\partial \Psi^*}{\partial x} \tag{1}$$

$$\frac{\partial u}{\partial x}+\frac{\partial v}{\partial y}=0 \tag{2}$$

Where F_x and F_y represent the effect of magnetic particles concentration on fluid in x and y direction, respectively.

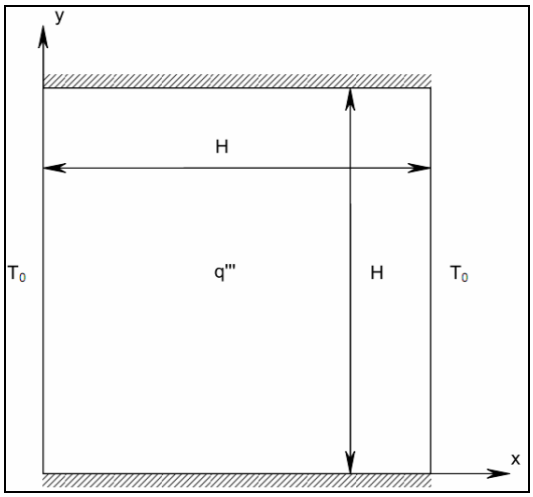

Figure 1: Position of Magnet to apply on Schematic of the square cavity with volumetric heat generation horizontal walls are adiabatic and vertical walls are isothermal

The nanoparticles can obtain with the method of Abdollahzadeh et al. [63]. After adding silver nitrate to Sargassum anustifolium extract, the brownish-yellow color in mixture turned in to dark brown color after 110 min (Figure 1). To make sure the synthesis of silver nanoparticles, nanoparticle absorption peak was measured using UV-visible spectrometer (UV-Vis) in the wavelength range of 200-700 nm. The best peak was observed after 2h of reaction time in the range of 406 nm, which corresponds to plasmon excitation of the AgNPs. The peak formed in this range represented reduction of silver ions and after synthesis of silver nanoparticles using extracts of seaweed Sargassum.The UV-V is absorption spectrum of silver nanoparticles synthesized by treating 1mM AgNO3 solution with Sargassum angustifolium extract [63]. According to the TEM analysis, average size of synthesized silver nanoparticles was 32.54nm and predominately spherical in shape (Figure 2).

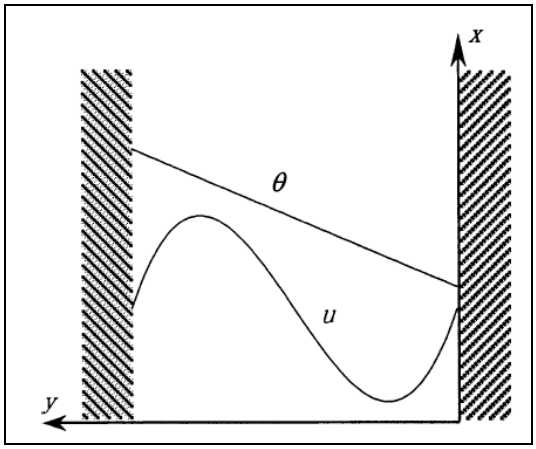

Figure 2: The physical description of problem [63]

As shown in [63], apart from the perfect spherical shape and size all particles dispersion was good and well–distributed in solution and is not in contact with each other. The viscous, steady, two-dimensional, incompressible, laminar biomagnetic fluid (blood) flow is considered as taking place through a forked artery with a stenosis. The

flow is subject to a magnetic source, which is located very close to the lower wall and below it. The flow at the entrance is expected to be fully developed and all the arterial walls are kept at a constant temperature, while the fluid is higher than wall. The origin of the Cartesian coordinate system is located at the leading edge of the lower wall. The volume force terms $(F_x \text{ and } F_y)$ are equal to the magnetic forces on a single particle at that location multiplied by the number of particles per unit volume by, n ($F_x = nF_{Mag-x}$). The magnetic force on single particle and F_x and F_y are as follows, respectively. The magnetophoretic force (FMAP) depends on the gradient of the magnetic intensity and the effective magnetic dipole moment (Meff) of the particles. It can be expressed as:

$$\rho\left(\mathrm{u}\frac{\partial u}{\partial x}+v\frac{\partial u}{\partial y}\right)=-\frac{\partial \mathrm{p}}{\partial x}+\mu\left(\frac{\partial^2 u}{\partial x^2}+\frac{\partial^2 u}{\partial y^2}\right) \tag{3}$$

$$\rho\left(\mathrm{u}\frac{\partial v}{\partial x}+v\frac{\partial v}{\partial y}\right)=-\frac{\partial \mathrm{p}}{\partial y}+\mu\left(\frac{\partial^2 v}{\partial x^2}+\frac{\partial^2 v}{\partial y^2}\right)+\rho\beta\left(T-T_0\right)g-\sigma B_0^2 u \tag{4}$$

$$\rho c_p\left(\mathrm{u}\frac{\partial T}{\partial x}+v\frac{\partial T}{\partial y}\right)=\mathrm{k}\left(\frac{\partial^2 T}{\partial x^2}+\frac{\partial^2 T}{\partial y^2}\right)+q''' \tag{5}$$

Where $\rho_{nf}=(1-\phi)\rho_f+\phi\rho_s$, $\mu_{nf}=\dfrac{\mu_f}{(1-\phi)^{2.5}}$, $(\rho c_p)_{nf}=(1-\phi)(\rho c_p)_f+\phi(\rho c_p)_s$

$k_{nf}=k_f\left\{\dfrac{k_s+2k_f-2\phi(k_f-k_s)}{k_s+2k_f+2\phi(k_f-k_s)}\right\}$ is considered to be an electrically conducting bio magnetic Newtonian fluid and is assumed to be Newtonian, since there is a very little variation of viscosity with the applied magnetic field. Although blood is suspension of particles and should be treated as a non-Newtonian flow, it is generally accepted that it behaves as a Newtonian flow in arteries with large diameters. Likewise, the rotational forces acting on the erythrocytes when entering and exiting the magnetic field are discarded (equilibrium magnetization). The walls of the channel are assumed electrically non-conducting and the electric field is considered negligible. Where in Eqs (4) and (5) C_V is volume concentration (number of particles per unit volume) and is as follow:

$$\begin{aligned}
&u=v=0\ , \quad T=T_0 \quad \text{at } x=0\\
&u=v=0\ , \quad T=T_0 \quad \text{at } x=H\\
&u=v=0\ , \quad \frac{\partial T}{\partial \mathrm{y}}=0 \quad \text{at } y=0\\
&u=v=0\ , \quad \frac{\partial T}{\partial \mathrm{y}}=0 \quad \text{at } y=H
\end{aligned} \tag{6}$$

Where C_{V0} is initial volume concentration that equal to 0.03 and non-dimensional volume concentration (C) is determined by [8]:

$$\frac{\partial \Psi^*}{\partial y}\frac{\partial \nabla^2\Psi^*}{\partial x}-\frac{\partial \Psi^*}{\partial x}\frac{\partial \nabla^2\Psi^*}{\partial y}=v\nabla^4\Psi^*-\beta g\frac{\partial T}{\partial x} \tag{7}$$

The magnetization process of red blood cell behaves like the following function, known as the Langevin function, which defines the variation of magnetization with magnetic field. In equation (7) velocity of particles, v_p is calculated by balancing the hydrodynamic and magnetic forces and is given by Stokes drag law [8]:

$$\frac{\partial \Psi^*}{\partial y}\frac{\partial T}{\partial x}-\frac{\partial \Psi^*}{\partial x}\frac{\partial T}{\partial y}=\alpha\nabla^2 T+\frac{q'''}{\rho c_p} \tag{8}$$

Where:

$$\Psi^*=\frac{\partial \Psi^*}{\partial x}=0 \quad T=T_0 \quad \text{at } x=0 \qquad 9a$$

$$\Psi^*=\frac{\partial \Psi^*}{\partial x}=0 \quad T=T_0 \quad \text{at } x=H \qquad 9b$$

$$\Psi^*=\frac{\partial \Psi^*}{\partial y}=0 \quad \frac{\partial T}{\partial y}=0 \quad \text{at } y=0 \qquad 9c \tag{9}$$

$$\Psi^*=\frac{\partial \Psi^*}{\partial y}=0 \quad \frac{\partial T}{\partial y}=0 \quad \text{at } y=H \qquad 9d$$

The externally applied magnetic field strength and the electrical conductivity of the blood are two most important parameters for the FHD and MHD problems. In order to study the effect of both of this two parameters we introduce, the concepts blood viscosity. Normally, the red blood cells occupy 35% to 50% of the blood. Therefore deformability, orientation and aggregation of red blood cells result in shear-thinning viscosity of the blood. For non-Newtonian behavior of the blood, its viscosity becomes a function of shear rate. Therefore a relation between viscosity and shear rate is required. The Relation between shear stress and shear rate is:

$$x=\frac{x^*}{H} \quad \Psi=\frac{\Psi^*}{\alpha}$$

$$x=\frac{\bar{x}}{\sqrt{v_f/a}}\ ,\ y=\frac{\bar{y}}{\sqrt{v_f/a}}\ ,\ u=\frac{\bar{u}}{\sqrt{av_f}}\ ,\ v=\frac{\bar{v}}{\sqrt{av_f}}\ ,\ \theta=\frac{T-T_\infty}{T_w-T_\infty}\ ,\quad \Pr=\frac{\nu}{\alpha}=\frac{\mu c_p}{k}\ , \tag{10}$$

$$Ra=\frac{\beta g q''' H^5}{\alpha \nu k}$$

In equation 10, the shear stress tensor is given by:

$$\frac{\partial \Psi}{\partial y}\frac{\partial \nabla^2 \Psi}{\partial x}-\frac{\partial \Psi}{\partial x}\frac{\partial \nabla^2 \Psi}{\partial y}=\Pr\nabla^4\Psi-\Pr Ra\frac{\partial \theta}{\partial x} \tag{11}$$

And the shear rate is given by:

$$\frac{\partial \Psi}{\partial y}\frac{\partial \theta}{\partial x}-\frac{\partial \Psi}{\partial x}\frac{\partial \theta}{\partial y}=\nabla^2\theta+1 \tag{12}$$

And viscosity is given by the power law model as follow [12]:

$$\frac{\partial^4\Psi}{\partial y^4}+2\frac{\partial^4\Psi}{\partial x^2\partial y^2}+\frac{\partial^4\Psi}{\partial x^4}=\frac{1}{\Pr}\left[\frac{\partial \Psi}{\partial y}\frac{\partial^3\Psi}{\partial x^3}+\frac{\partial \Psi}{\partial y}\frac{\partial^3\Psi}{\partial y^2\partial x}-\frac{\partial \Psi}{\partial x}\frac{\partial^3\Psi}{\partial y^3}-\frac{\partial \Psi}{\partial x}\frac{\partial^3\Psi}{\partial x^2\partial y}\right]+Ra\frac{\partial \theta}{\partial x} \tag{13}$$

And viscosity is given by the power law model as follow [12]:

$$\frac{\partial^2\theta}{\partial x^2}+\frac{\partial^2\theta}{\partial y^2}=\frac{\partial \Psi}{\partial y}\frac{\partial \theta}{\partial x}-\frac{\partial \Psi}{\partial x}\frac{\partial \theta}{\partial y}-1 \tag{14}$$

where values for m and n are given in Table 1. In our study if viscosity that is calculated from power law model (Eq. 13) becomes greater than μ_{Max}(0.02) or smaller than μ_{Min}(0.00309), the calculated values are replaced by maximum or minimum value. All other parameters are given in Table 1.

Table 1: Uncertainty analysis

Items	Maximum value	Accuracy
Measured parameters		
Temperature (K)	348.4	±2 K for the IR ±0.6 K for the thermocouples
Pressure difference (Pa)	2080	±3 Pa
Velocity (m/s)	15.5	±3% for 0.3–3 m/s ±1% for 3.1–35 m/s
Electric voltage (volt)	1.67	±1%
Electric current (Ampere)	7	±2%
Emissivity	0.82	±0.02
For all of the dimensions (mm)	105	±0.02 mm
Calculated parameters		Mean total uncertainty (%)
Air mass flow rate, m (kg/s)	0.0107	1.73
Reynolds number, Re (–)	24,423	3
Nusselt number, Nu (–)	1494	3.15
pomp power, Wp (W/m2)	8375	3.1
Pressure gradient, dP/dz (Pa/m)	30,952	9.6

A finite volume code is developed and utilized. At the inlet to the vessel dimensionless concentration is equal to 1, see Figure 1. Also, at the exit of the vessel Neumann boundary condition is applied. Furthermore the upper and lower walls are insulated. In addition the diffusion coefficient (D) is equal to $1 \times 10^{-9} \frac{m^2}{s}$ [6]. A thin, straight wire carrying a current is placed along the x-axis, as shown in Figure 1. Evaluate the magnetic field at any internal points. Note that we have assumed that the leads to the ends of the magnet make call off contributions to the net magnetic field at any internal point.

RESULTS AND DISCUSSION

It is well known from experimental studies, failures caused by test system design due to inclined flow channel, leaks in the test section, inaccurate estimation of roughness, failure to locate the pressure taps as a perpendicular at the channel surface, the absence of a personal error in the temperature measurement may result in significant deviations in the experimental findings. The most convenient way of determining the presence of these types of negative effects is to compare the experimental findings with the appropriate references in the literature.

Firstly, the data obtained from the experiments were compared with Petukhov's and Gnielinski's correlations for an empty flat plane channel flow. The local Nusselt number based on the channel height (NuHi) was obtained by Eq. (13). The NuHi values are given in Fig. 6 at the different ReH values. As can be seen the value of the local Nusselt number is quite consistent (maximum of 9%) with theoretical values at ReH = 24,423. When the average values of the Nusselt number are compared with the theoretical NuH in range of 3000 < ReH < 5000, the maximum difference is observed as 72% (Fig. 7). The reason for this, the experimental and theoretical values in the transition zone are not meeting each other exactly. The effect of the transition region from laminar to turbulent flow decreases laminar and the differences between the experimental and theoretical values becomes a maximum of 12%. The empirical data agree with the data obtained from the correlations of Gnielinski and Dittus–Boelter correlation when NuH was taken into consideration.

As it is known, the local Nusselt number starts with the highest value proportionally with the Reynolds number and obtains a fixed value at the thermal and hydrodynamic fully developed regions. Similar behavior is observed in the higher value of heat transfer in the porous media. However, pressure drop is also relatively high. The present study investigated the heat performance of a flow system in which there is partially filled porous media at the inlet of channel, but low pressure drops. In addition, the effect of porous media partially filled by open porous aluminum

foam at the channel inlet on heat transfer, and the pressure drop are determined. Different positions of aluminum foam material parallel to flow direction were investigated in the flow region which is thermally developing on the inlet of the channel.

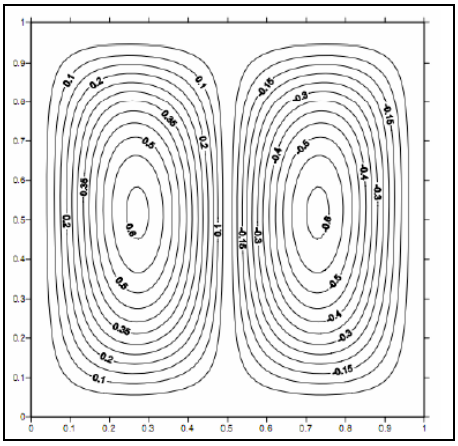

Figure 3: Contour for an internally heated square enclosure with adiabatic horizontal walls and isothermal vertical walls at *Ra* =10000

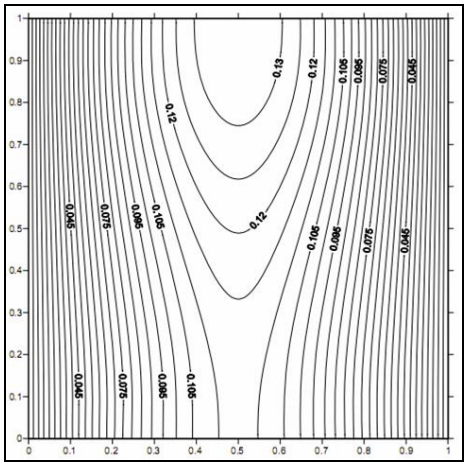

Figure 4: Thermal component in 1 mm/s velocity

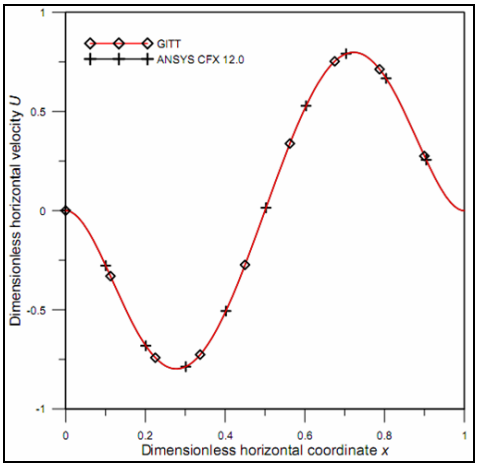

Figure 5: Real picture of common carp (Cyprinus carpio)

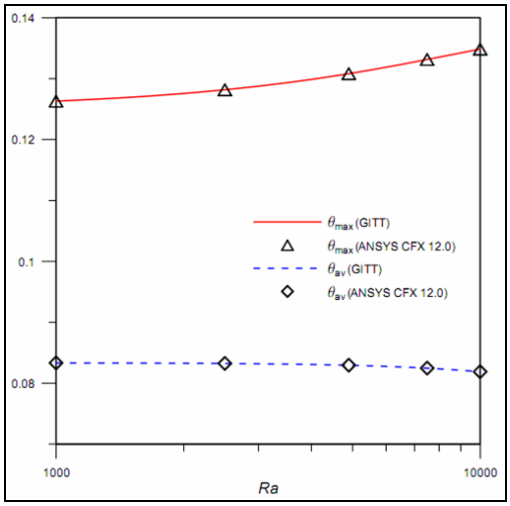

Figure 6: Real picture of common carp (Cyprinus carpio)

Therefore, it was aimed to increase heat transfer by forming porous media in the inlet of channel, however it was attempted to acquire a lower drop in pressure. It is clear that heat transfer would be higher in the case k = 0 (full-filled) considering the present study. Previous studies have not dealt with fill rate and aluminum foam shape to show the increase in the heat transfer amount. When viewed from this angle, this study makes an original contribution to the literature. Extensive research has been carried out on the state of fully filled varying section channels with aluminum foam and the results obtained from the channel flow with fully filled aluminum foam are compatible with many of these studies. The NuR = (NuH,p/NuH,emp) ratio gives the rate of the porous channel Nusselt number to the experimental empty channel Nusselt number. As can be seen, for laminar channel flow, the porous media heat transfer increases relatively according to the empty channel with the increment of the ReH for both 10 PPI and 20 PPI (Fig. 11). Pressure parameter "τ" increases linearly at the Forchheimer flow regime according to the Muskat's flow regime model. Here, we know that the pressure gradient is proportional to the heat transfer. However, the experiments show that flow regime also has a different effect on heat transfer. For the laminar channel flow, the effect inertial forces on heat transfer increases with increasing the ReH according to the empty channel flow in porous media. Even so, the increment in heat transfer becomes at a maximum value in the upper limit (ReH ≈ 2200) of the laminar flow. Then, the channel flow regime passes to turbulent flow by increasing the ReH and the inertial effects on the empty channel reduces according to the porous medium. This reduction trend is inversely proportional to the k value. These findings demonstrate similar behavior for both 10 PPI and 20 PPI. As can be seen, the effect of the k on the NuR decreases with increasing the ReH for 10 PPI and the heat transfer increment rate becomes an equal and constant value particularly k > 0. However, the effect of the ReH on the increment rate continues for 20 PPI. This situation demonstrates that the thermal input length is different for both two pore densities. In addition, the experimental findings show the NuH value changes little according to the ReH and has approximately equal value at k ⩾ 1 for 10 PPI. It shows that the flow that is headed to the free flow region leaves the test region in the upper channel part. It is thought that the experiments should be repeated by increasing the L/L+ value in steady L+ value for a better physical explanation of this phenomena. There is also a direct proportion between the pore density and the NuR. As seen from Fig. 11 and Fig. 10, k = 0 for ReH < 2200 and the NuR value becomes average 20 for 10 PPI while average 27 for 20 PPI. In addition to this, the NuR value is 8 and 9 at k = 0.5 for 10 PPI and 20 PPI, respectively. These rates are slightly less value than the laminar flow to the turbulent channel flow channel.

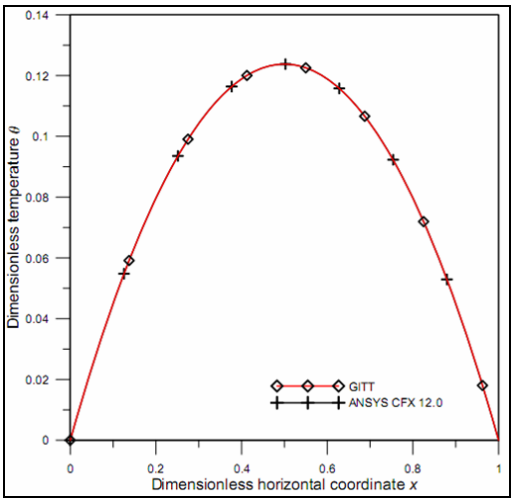

Figure 7: Mesh of blood vessel

The change of local Nusselt number (NuHi) for 10 PPI and 20 PPI aluminum foam along the channel is given in Fig. 9 and Fig. 10. As seen the value of the NuHi increases with the increasing value of the ReH. Here, two important findings will be examined. One of them is the Reynolds number. In this study, each of the Reynolds numbers is examined for both laminar and turbulent flow. These values of ReH = 2193 and ReH = 2930 show the approximate boundaries of an overall transition region for internal flows. As is known, heat transfer significantly increases when the flow regime passes from laminar flow to turbulent flow in an empty channel flow with the effect of inertial forces. As shown in Fig. 9, the NuHi value increases about 25–40% rate through the channel when the value of the Reynolds number rises from 2193 to 2930 for 10 PPI. Despite that, the NuHi increases the average 15–25% in this transition zone for 20 PPI. As can be seen, the increment rate for 10 PPI is relatively greater than the increment obtained for 20 PPI. Hence, it is concluded that the effect of the inertial force is closer to low pore density in the thermal development region. As seen from Fig. 9 and Fig. 10, the height of the selected aluminum foam is not sufficient to provide a thermal development region. Another important finding is instabilities in the NuHi values.

As shown, the instability of the NuHi increases with the increasing value of the ReH for both pore densities. Approximately the same results were obtained in the repeating experiments.

Approximately 300 temperature measurements were obtained along the 105 mm test section. So, 3 temperature values are read about every 1 mm. It gives more precise results for the surface temperature according to this surface temperature measured by the thermocouple. As can be seen, the pore density is directly proportional with amplitude however, inversely proportional with the wavelength of the resulting instabilities. This shows that heat transfer is proportional to the pore density in the porous media. In addition, instability amplitude seen in thermal development region increases for both 10 and 20 PPI as value of the Reynolds number increases. However, the instability wavelength does not change. Following conclusions could be drawn: wavelength is associated with contact density with the heating surface of porous material. Thus, the extended surface effect of the porous structure increases as the Reynolds number increases, and this situation reveals the result in increasing amplitude. It is a known scientific status. It shows the importance of contact resistance between porous media and channel surface in porous flow media. Namely, it concluded that it is very important to maximize the pore density of an extended surface in porous media.

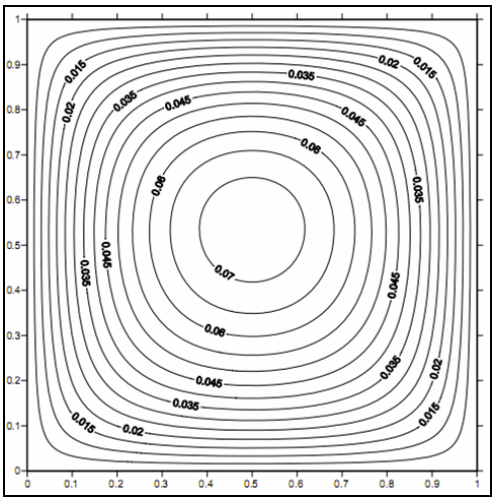

Figure 8: Velocity component, pressure, and particle concentration at t = 0.1 (s)

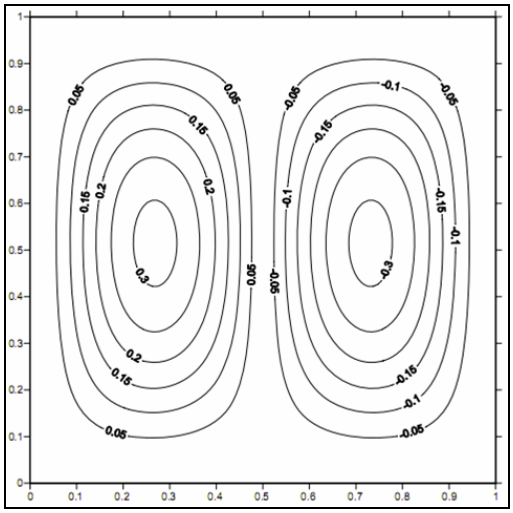

Figure 9: Velocity component, pressure, and particle concentration at t = 1 (s)

As is known, the heat transfer performance in porous media depends on the Reynolds number (2uR/t), the geometrical parameters of the metal foam (R/dp), porosity (εp), and the ratio of liquid-solid thermal conductivity (λf/λs) [23].

Here, the Reynolds number is a dimensionless number used in determining the porous media flow regime. If the Reynolds number is low, the Darcy regime is valid. Conversely, the Forchheimer regime is valid for a high Reynolds number. The flow regime in a porous media is divided into three regions by Muskat [29].

The first zone called the Darcy region in which the change is too small (Fig. 8). The second is the transition zone and the third region is a region that is dominated by inertia forces and thereby nonlinear effects.

This region contains the non-Darcy flow and Forchheimer flow regime. In this study, as it is seen from Figure 8, the ($\tau = (Rea\Delta P/\rho V2)$) value increases depending on the Reynolds number (Rea) due to the flow rate which is too high.

The solution of (10)-(14) is

$$\theta(\eta)=1-\frac{\int_0^{\eta}\exp(\frac{-m\tau-\exp(-m\tau)}{Am^2})d\tau}{\lim_{\tau\to\infty}\left\{\int_0^{\tau}\exp\left(\frac{-m\tau-\exp(-m\tau)}{Am^2}\right)d\tau\right\}}$$

$$\theta'(0)=\frac{-\exp(\frac{-1}{Am^2})}{\lim_{\tau\to\infty}\left\{\int_0^{\tau}\exp\left(\frac{-m\tau-\exp(-m\tau)}{Am^2}\right)d\tau\right\}}$$

$$\frac{1}{\Pr}\frac{1}{\left[1-\phi+\phi(\rho c_p)_s/(\rho c_p)_f\right]}\left(\frac{k_{nf}}{k_f}\right)m^2\left[\xi\theta''+\theta'\right]+(\xi-1)\theta'=0$$

$$\theta(1)=1,\quad \theta(0)=0$$

$$\theta(\xi)=\frac{-B_3}{B_5}\frac{\exp\left(\frac{2-\xi}{2Am^2}\right)}{\xi^{1+B_2/2}}\left\{\begin{array}{l}Am^2(\xi+Am^2+1)Whitta\ker M(\frac{-B_2}{2},\frac{1+B_1}{2},\frac{\xi}{Am^2})\\+B_4 Whitta\ker M(\frac{-B_1}{2},\frac{1+B_1}{2},\frac{\xi}{Am^2})\end{array}\right\} \quad (15)$$

$$A=\frac{1}{\Pr}\frac{1}{\left[1-\phi+\phi(\rho c_p)_s/(\rho c_p)_f\right]}\left(\frac{k_{nf}}{k_f}\right),\quad B_1=\frac{Am^2+1}{Am^2},\quad B_2=\frac{Am^2-1}{Am^2}$$

$$B_3=(Am^2)^{2+B_1/2}(1+3Am^2),\quad B_4=1+2Am^2+A^2m^4$$

$$B_5=\left\{B_6\Gamma(1+B_1,\frac{1}{Am^2})-B_7\Gamma(2+B_1)\right\}\exp(\frac{1}{Am^2})-A^2m^4(2+Am^2)hypergeom([2],[3+B_1],\frac{1}{Am^2})$$

$$B_6=(Am^2)^{1+B_1}(1+9Am^2+34A^3m^6+12A^4m^8+28A^2m^4)$$

$$B_7=(Am^2)^{2+B_1}(1+14A^2m^4+6A^3m^6)$$

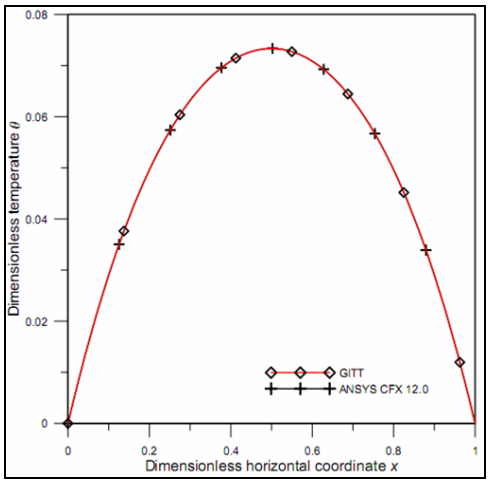

Figure 10: Velocity component, pressure, and particle concentration at t = 2 (s)

CONCLUSION

In the present study, the heat transfer and pressure drop in a rectangular channel (exposed to the constant heat flow) of fully/partially filled open pore aluminum foam were investigated. 10 PPI and 20 PPI aluminum foam materials were placed into the channel arranged in a way to be fully or partially filled with different shapes against the flow direction. The experiments were performed in a wide range of the Reynolds numbers ($893 \leqslant ReH \leqslant 24{,}423$) and in the Forchheimer flow regime. Air was selected as working fluid. Based on the experiments, the following remarkable conclusions are presented:

Heat transfer and pressure drop is proportional to the pore density and the Reynolds number, and is inversely proportional to k parameter.

The heat transfer increases in the channel with increasing the filling rate of the aluminum foam and decreasing the free flow area.

The effect of the Reynolds number on both heat transfer (NuH) and pressure gradient ($-dP/dz$) decreases for all pore densities in the case of $k > 0$. Also at all Reynolds numbers, the effect of the k on the heat transfer and pressure drop decreases except for $k = 0$.

It is seen that the HTC is better for 10 PPI according to 20 PPI at a constant pump power.

According to the TEF assessment, low pore density structure should be preferred at a low Reynolds number, hence low pump power (Wp) in a fully filled ($k = 0$) channel flow. Apart from this, low pore density structure should be preferred at all Reynolds number for $k > 0$.

According to the experiment results, it was seen that since the air prefers to go through the free flow zone, the heat transfer decreased as a result of decreasing the flowing mass flow rate in the porous medium. Therefore, for $h+ = 5$ value, $k \geqslant 1$ should not be preferred in order to acquire and efficient heat transfer.

It is concluded that fluid inlet conditions should be investigated in a wider context with regards to h+/H and L+/L in order for these findings to contribute to the literature and application areas.

ACKNOWLEDGEMENTS

The author is grateful to Dr MY Abdollahzadeh Jamalabadi for her guidance.

REFERENCES

[1] MY Abdollahzadeh Jamalabadi, *J. Porous Media*, **2015**, 18(9), 843-860.
[2] MY Abdollahzadeh Jamalabadi; JH Park, *Therm. Sci*., **2014**, 94-94
[3] MY Abdollahzadeh Jamalabadi, *Int. J. Opt. Appl*., **2015**, 5 (5), 161-167
[4] MY Abdollahzadeh Jamalabadi, *Chem. Eng. Res. Des*., **2015**, 102, 407-415
[5] MY Abdollahzadeh Jamalabadi ; JH Park, *World App. Sci. Journal*, **2014**, (4)32, 672-677
[6] MY Abdollahzadeh Jamalabadi; JH Park ; CY Lee, *entropy*, **2015**, 17 (2), 866-881
[7] A Shahidian; M Ghassemi; S Khorasanizade; M Abdollahzade; G Ahmadi, *IEEE Trans. Magn*., **2009**, 45 (6)2667-2670
[8] MY Abdollahzadeh Jamalabadi, *J. Marine Sci. & App*, **2014**, 13 (3) 281-290
[9] MY Abdollahzadeh Jamalabadi ; JH Park, *Int. J. Sci. Basic App. Res. Sci.* 1, **2014**, 421-427
[10] MY Abdollahzadeh Jamalabadi ; JH Park, *Open J. Fluid Dyn.*, **2014**, 23 (4) 125-132
[11] MY Abdollahzadeh Jamalabadi; JH Park*; MM Rashidi ; JM Chen, J. Hydrod. Ser*. B, **2016**
[12] MY Abdollahzadeh Jamalabadi, *Front Heat Mass Trans*., **2015**, 6, 013007
[13] M.Y. Abdollahzadeh Jamalabadi, *J. Fuel Cell Sci. Technol*., **2013**, 10(5), 1039
[14] MY Abdollahzadeh Jamalabadi; JH Park; CY Lee, *Therm. Sci.*, **2014**, 124-124
[15] M Jamalabadi; P Hooshmand; B Khezri ; A Radmanesh, *Ind. J. sci. Res*. 2, **2014**, 74-81
[16] MY Abdollahzadeh Jamalabadi, *Mul. Model Mat. Struc*., **2016**
[17] MY Abdollahzadeh Jamalabadi, JH Park; CY Lee, *Int J Appl Environ Sci*, **2014**, 9 (4) 1769-1781
[18] MY Abdollahzadeh Jamalabadi, *World App. Sci.* J., **2014**, 32 (4), 667-671
[19] MY Abdollahzadeh Jamalabadi, *Mid-East J. Sci. Res*., **2014**, 22 (4), 561-574
[20] MY Abdollahzadeh Jamalabadi, *Mat. Perf. Char*., **2015,** 20140062.
[21] MS Shadloo; R Poultangari; MY Abdollahzadeh Jamalabadi, MM Rashidi, *Energ Convers Manage*, **2015**, 96, 418-429.

[22] MY Abdollahzadeh Jamalabadi; M Ghasemi; MH Hamedi, *Int. J. Numer Meth Heat Fluid Flow*, **2013**, 23 (4), 649-661.
[23] MY Abdollahzadeh Jamalabadi, *Int. J. Ener. Mat. Chem. Pro.* , **2016**, 15,
[24] MY Abdollahzadeh Jamalabadi, *Noise and Vibration Worldwide*, **2014**, 45 (8), 21-27.
[25] MY Abdollahzadeh Jamalabadi, *J. King Saud Univ. Eng. Sci.*, **2014**, 26 (2), 159-167.
[26] MY Abdollahzadeh Jamalabadi ; M Ghasemi ;MH Hamedi, *Proc. Inst. Mech. Eng., Part C, J. Mech. Eng. Sci.,* **2012**, 226, 1302-1308.
[27] MY Abdollahzadeh Jamalabadi, *Int. J. Ener. Eng.*, **2015**, 5(1), 1-8.
[28] MY Abdollahzadeh Jamalabadi, *Int. J. Mult. Res. Dev*., **2014**, 5 (1), 1-4.
[29] S Dousti; J Cao; A Younan; P Allaire; T Dimond, *J. tribology*, **2012**, 134 (3), 031704.
[30] S Dousti; JA Kaplan, F He; PE Allaire, *ASME Turb. Exp. Conf.* , **2013**.
[31] F He; PE Allaire; S Dousti; A Untaroiu, *ASME Int. Mech. Eng. Cong. Exp*., **2013**.
[32] S Dousti; RL Fittro, *ASME Turb. Exp. Conf.* , **2015**.
[33] E Sarshari; N Vasegh;M. Khaghani; S Dousti, *ASME Int. Mech. Eng. Cong. Exp.,* **2013**.
[34] S Dousti; TW Dimond; PE Allaire, HE Wood, *ASME Int. Mech. Eng. Cong. Exp.*, **2013**.
[35] S Dousti;MA Jalali, *J. App. Mech*., **2013**, 80 (1), 011019.
[36] YG Sun; B Mayers; YN Xia, *Nano Lett*., **2003**, 3, 675–679.
[37] V Venkatpurwar; V Pokharkar, *Mater Lett*, **2011**, 65, 999–1002.
[38] R Patakfalvi; Dekany, *Colloid Polym. Sci*., **2010**, 280, 461–470.
[39] P Kumar; Senthamil SS; A Lakshmi Prabha; K Prem Kumar; RS Ganeshkumar; M Govindaraju, *Nano Biomed Eng*, **2012,** 4, 2-16.
[40] P Mansuya; P Aruna; S Sridhar; JS Kumar; S Babu, *J Exp. Sci*., **2010**, 1, 23-26.
[41] K Fent, *Ecotoxicol Enginee Nanoparticles*, **2010**, 183-205.
[42] M Alishahi; M Mesbah; M Ghorbanpoor, *Iranian J. Veterinary Res*., **2011**, 7, 36-41.
[43] PV Asharani; YL Wu; Z Gong; S Valiyaveettil, *Nanotechnol*, **2008**, 19, 1–8.
[44] K Bilberg; MB Hovgaard; F Besenbacher; E Baatrup, *J. Toxicol*, **2012**, 293784, 1-9.
[45] K Bilberg; H Malte; T Wang; E Baatrup, *Aquatic Toxicol*, **2012**, 96, 159-165.
[46] G Singaravelu; JS Arockiamary; KV Ganesh; K Govindaraju, *Colloids Surf. Biointerfaces*, **2007**, 57, 97-101.
[47] P Jegadeeswaran; R Shivaraj; R Venckatesh, *Digest J. Nanomaterials Biostructures*, **2012**, 7, 991 – 998.
[48] QA Pankhurst; NK T Thanh; SK Jones; and J Dobson, *J. Phys. D: Appl. Phys.*, **2003**, 36(13), 167–181.
[49] L Johannsen; J O Blanchette, *Adv. Drug Deliv*., **2004**, 56, 1649–1659.
[50] M E Davis; Z Chen; D M Shin, Nat. Rev. *Drug. Discov*., **2008**, 7, 771–782.
[51] M Arruebo; R Fernandez-Pacheco; M R Ibarra; J Santamaria, *Nano Today*, **2007**, 2, 22-32.
[52] C Alexiou; R Jurgons; C Seliger; O Brunke; H Iro; S Odenbach, *Anticancer Res*., **2007**, 27(4A), 2019–2022.
[53] S I Takeda; F Mishima; S Fujimoto; Y Izumi; S Nishijima, *J. Magn. Mater.*, **2006**, 311, 367-371.
[54] K B Yesin; K lmers; B J Nelson, *Int. J. Robot. Res*, **2006**, 25, 527-536.
[55] J J Abbott; O Ergeneman; M P Kummer; A M Hirt; B J Nelson, *IEEE Trans. Robot*., **2007**, 23, 1247-1252.
[56] C Alexiou; D Diehl; P Henninger; H Iro; R Rockelein; W Schmidt; H Weber, *IEEE Trans. Appl. Supercond*., **2006**, 16, 1527–1530.
[57] X Han; Q Cao; and L Li, *IEEE Trans. Appl. Supercond*., 2012, 22(3), 4401404– 4401404.
[58] J-B Mathieu; S Martel, *Biomed. Microdevices*, **2007**, 9, 801–808.
[59] S Martel; O Felfoul; J-B Mathieu; A Chanu; S Tamaz; M Mohammadi; M Mankiewicz; N Tabatabaei, *Int. J. Rob. Res.*, **2009**, 28(9), 1169–1182.
[60] H Choi; J Choi; G Jang; J Park; S Park, *Smart Mater. Struct.*, **2009**, 18(5), 055007.
[61] S Jeon; G Jang; H Choi; S Park, *IEEE Trans. Magn.*, **2010**, 46(6), 1943–1946.
[62] H Choi; K Cha; J Choi; S Jeong; S Jeon; G Jang; J Park; S Park, *Sens. Actua. A: Phys*., **2010**, 163(1), 410–417.
[63] M Y Abdollahzadeh Jamalabadi, *J. Chem. Pharm. Res.*, **2015**, 7(11), 91-98.